Inorganic Chemistry

Article

pubs.acs.org/IC

Disorder–Order Transformation and Significant Dislocation Motion Cooperating with a Surprisingly Large Hysteretic Magnetic Transition in a Nickel–Bisdithiolene Spin System

Hai-Bao Duan,[†] Xuan-Rong Chen,[†] Hao Yang,[†] Xiao-Ming Ren,*[,†,‡] Fang Xuan,[†] and Shi-Ming Zhou*[,§]

[†]State Key Laboratory of Materials-Oriented Chemical Engineering and College of Science, Nanjing University of Technology, Nanjing 210009, People's Republic of China

[‡]State Key Laboratory & Coordination Chemistry Institute, Nanjing University, Nanjing 210093, People's Republic of China

[§]Hefei National Laboratory for Physical Sciences at Microscale, University of Science and Technology of China, Hefei, Anhui 230026, People's Republic of China

Supporting Information

ABSTRACT: The compound [4′-CF_3bzPy][Ni(mnt)$_2$] (**1**) (where 4′-CF_3bzPy = 1-(4′-(trifluoromethyl)benzyl)pyridinium and mnt^{2-} = maleonitriledithiolate) was synthesized and displays a magnetic bistability with a surprisingly large thermal hysteresis loop (~49 K). X-ray crystallographic studies reveal that in the high-temperature (HT) phase the anions and cations form mixed stacks, with alternating anion dimers (AA) and cation dimers (CC) in an ...AACCAACC... fashion along the crystallographic $a + b$ direction, and disordered CF_3 groups in the cations are aligned into a molecular layer parallel to the crystallographic (001) plane. However, in the low-temperature (LT) phase, the c-axis length of the unit cell is roughly doubled, and the asymmetric unit switches from one [4′-CF_3bzPy][Ni(mnt)$_2$] pair in the HT phase to two [4′-CF_3bzPy][Ni(mnt)$_2$] pairs. Most interestingly, the CF_3 group in the cations becomes ordered, and the conformation of one of two crystallographically different cations changes significantly. A dislocation motion between the neighboring molecular layers emerges as well. The analyses of the magnetic susceptibilities and the density functional theory calculations suggest that the antiferromagnetic exchange interaction within one of two types of $[Ni(mnt)_2]_2^{2-}$ dimers in the LT phase is much stronger than that within the $[Ni(mnt)_2]_2^{2-}$ dimer in the HT phase. The lattice reorganization during this phase transition is proposed to be responsible for the wide thermal hysteresis loop.

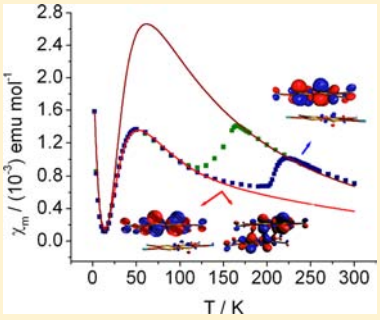

INTRODUCTION

Functional materials with bistable (or hysteresis) behavior on the molecular scale are in large demand in electronic and photonic technologies.[1] Generally, magnetic bistability is observed in spin-crossover (SCO) complexes,[2−5] valence tautomeric compounds,[6] and one-dimensional (1-D) $S = 1/2$ spin-Peierls-type transition compounds.[7] The transition temperature T_C and the hysteresis loop width ($\Delta T_C = T_C\uparrow - T_C\downarrow$) for a magnetically bistable compound are technologically important parameters for practical applications, and the 50 K and more width of the loop and it being centered at near room temperature are thought to be necessary for high-density storage media.[1a]

For a magnetic bistable compound with a wide hysteresis loop, it is necessary to strengthen cooperative interactions between the spin-active units in the lattice. It has been observed that an absence of strong intermolecular interactions between spin-active centers (polymeric units) results in a low cooperativity in the SCO complex.[10] Therefore, a general strategy for this purpose is to enhance the lattice rigidity by using covalent linkers to[8] or promoting the noncovalent interaction (such as H-bonding, π stacking, guest inclusion, van der Waals forces, and so on) between[9] the spin-active units. On the other hand, it is worthy of noting that the disorder-to-order transformation can provide an intrinsic impulse for the initiation of the spin transition. By coupling the magnetic transition to the disorder–order transformation rather than strengthening intermolecular interactions, magnetic bistability with large hysteresis loops was observed in the unsymmetrical dithiolene complexes [Cp_2M][Ni(tfadt)$_2$] (Cp = cyclopentadiene; M = Fe or Co; tfadt = (trifluoromethyl)acrylonitrile-1,2-dithiolate), in which the disorder–order transformations of the spin-inactive components, CF_3 and cyclopentadienyl groups, are coupled with the magnetic bistability.[11]

In this paper, we present a novel example that a π-type dimer compound, [4′-CF_3BzPy][Ni(mnt)$_2$] (**1**) (4′-CF_3BzPy = 1-(4′-(trifluoromethyl)benzyl)pyridinium; mnt^{2-} = maleonitriledithiolate), exhibits magnetic bistability with a ca. 49 K thermal hysteresis loop. It was confirmed that the magnetic bistability in such a dimer system is coupled with the disorder–order transformations of the CF_3 group in the spin-inactive cation and the dislocation motion of the neighboring molecular layers.

Received: November 24, 2012
Published: March 21, 2013

Table 1. Crystal Data and Structural Refinement of 1

	293 K	190 K	160 K	131 K
chemical formula		$C_{21}H_{11}F_3N_5NiS_4$		
fw	577.30	577.30	577.30	577.30
wavelength (Å)	0.71073	0.71073	0.71073	0.71073
CCDC number	911452	911453	911454	911455
cryst syst	triclinic	triclinic	triclinic	triclinic
space group	$P\bar{1}$	$P\bar{1}$	$P\bar{1}$	$P\bar{1}$
a (Å)	8.3497(13)	8.2623(6)	8.2247(4)	8.5682(8)
b (Å)	11.6251(19)	11.5851(6)	11.5827(4)	11.4127(9)
c (Å)	13.813(2)	13.8576(9)	13.8825(7)	25.008(2)
α (deg)	71.189(3)	71.043(5)	70.995(4)	96.294(7)
β (deg)	75.117(3)	74.970(6)	74.753(4)	93.068(7)
γ (deg)	77.007(3)	77.509(5)	77.577(4)	103.850(7)
V (Å^3)/Z	1211.7(3)/2	1198.87(13)/2	1194.18(9)/2	2352.0(4)/4
density (g·cm^{-3})	1.582	1.599	1.605	1.599
abs coeff (mm^{-1})	1.188	1.201	1.206	1.223
F(000)	582.0	582.0	582.0	1120.0
data collection θ range (deg)	1.59−26.00	2.82−29.25	2.98−28.99	2.02−29.20
index range	$-10 \le h \le +9$	$-10 \le h \le +11$	$-10 \le h \le +10$	$-8 \le h \le +11$
	$-12 \le k \le +14$	$-14 \le k \le +15$	$-14 \le k \le +14$	$-8 \le k \le +15$
	$-12 \le l \le +17$	$-17 \le l \le +17$	$-18 \le l \le +15$	$-31 \le l \le +31$
no. of reflns collected	6916	5618	5456	7427
no. of independent reflns	4716	3658	3559	3817
no. of data/restraints/params	4716/0/335	5618/0/335	5456/0/335	7424/0/613
goodness-of-fit on F^2	0.918	0.928	0.905	1.080
final R indices[a] [$I > 2\sigma(I)$]	R1 = 0.0583	R1 = 0.0552	R1 = 0.0359	R1 = 0.1171
	wR2 = 0.1387	wR2 = 0. 1378	wR2 = 0.0865	wR2 = 0.3060

[a] $R1 = \sum(||F_o| - |F_c||)/\sum|F_o|$. $wR2 = \sum w(|F_o|^2 - |F_c|^2)^2/\sum w(|F_o|^2)^2]^{1/2}$.

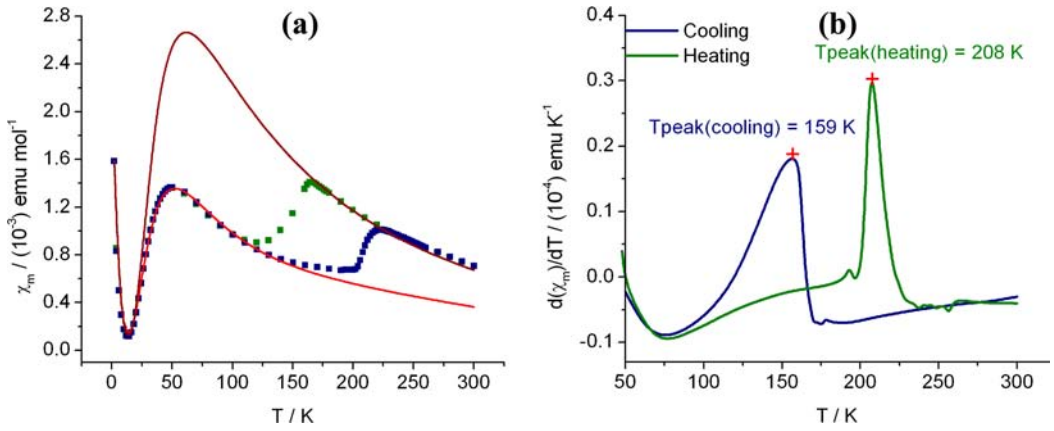

Figure 1. (a) χ_m vs T, where the solid squares and lines represent the experimental data and theoretically reproduced magnetic susceptibility data, respectively. (b) dχ_m/dT vs T in the cooling (green) and warming (blue) modes for **1**.

EXPERIMENTAL SECTION

Chemicals and Materials. The starting materials Na_2mnt[12] and [4′-CF_3bzPy]I[13] were synthesized using the methods described in the literature, and [4′-CF_3bzPy]$_2$[Ni(mnt)$_2$] was prepared employing a procedure similar to that reported in the literature.[13]

Physical Measurements. Elemental analyses for C, H, and N were performed with an Elementar Vario EL III analytic instrument. Powder X-ray diffraction (PXRD) data were collected on a Bruker D8 diffractometer with Cu Kα radiation (λ = 1.54018 Å). FT-IR spectra were recorded on an IF66 V FT-IR (4000−400 cm^{-1}) spectrophotometer with KBr pellets. Differential scanning calorimetry (DSC) was carried out on a Pyris 1 power-compensation differential scanning calorimeter in the range of 98−298 K (from −175 to +25 °C) for **1**, and the warming/cooling rate was 10 K·min^{-1} during the thermal cycles. Magnetic susceptibilities were measured on a Quantum Design MPMS-5 superconducting quantum interference device (SQUID) magnetometer over the temperature range of 2−300 K.

Preparation of a Sample of [4′-CF_3bzPy][Ni(mnt)$_2$]. A MeOH solution (10 cm^3) of I_2 (205 mg, 0.80 mmol) was slowly added to a MeCN solution (25 cm^3) of [4′-CF_3bzPy]$_2$[Ni(mnt)$_2$] (573 mg, 1.0 mmol), and the mixture was allowed to stand overnight after being stirred for 25 min. The dark powder formed was filtered off, washed with MeOH, and dried in a vacuum. Yield: ∼69%. Anal. Calcd for $C_{21}H_{11}F_3N_5NiS_4$: C, 43.69; H, 1.92; N, 12.13. Found: C, 43.76; H, 1.78; N, 12.25.

Crystals of **1** suitable for single-crystal X-ray diffraction can be obtained by slow evaporation of the saturated acetonitrile or acetone solution of the above powdered sample at ambient temperature for 5−7 days.

X-ray Crystallography. Selected crystals of **1** were centered on an Oxford Diffraction Xcalibur diffractometer equipped with a Sapphire 3

dx.doi.org/10.1021/ic302571p | Inorg. Chem. 2013, 52, 3870−3877

charge-coupled device (CCD) detector and graphite-monochromated Mo Kα radiation (λ = 0.71073 Å). Measurements were performed at 293, 190, 160, and 131 K for **1** (cooling mode). Note that it is really difficult to obtain good single-crystal X-ray diffraction data in the low-temperature phase since the crystal is often broken below ~160 K upon cooling. Single-crystal X-ray diffraction data at 131 K were finally successfully collected by slow cooling of the selected crystal at a rate of 2 K/h; even so, the crystal was broken into parts in the subsequent heating process.

The data collection routine, unit cell refinement, and data processing were carried out with the program CrysAlis.[14] Structures were solved by the direct method and refined by the full-matrix least-squares procedure on F^2 using the SHELXL-97 program.[15] The non-hydrogen atoms were anisotropically refined using the full-matrix least-squares method on F^2. Disorder models for the CF_3 group were used in the structure refinements of **1** at 293, 190, and 160 K. Each CF_3 group was assumed to have two possible sites, and the occupied factors for each site were refined. The crystallographic details on the data collection and structural refinement are summarized in Table 1.

Density Functional Theory (DFT) Calculation Details. All DFT calculations were carried out utilizing the Gaussan98 program[16] on an SGI 3800 workstation. The calculations for the single-point energy of the broken-symmetric (BS) singlet states of $[Ni(mnt)_2]_2^-$ spin dimers at the ubpw91/lanl2dz level[17−22] were performed on the non-modelized molecular geometry from the single-crystal X-ray analyses, and the SCF convergence criterion was 10^{-8}.

RESULTS AND DISCUSSION

Variable-Temperature Magnetic Susceptibility. The temperature dependence of the magnetic susceptibility of **1** measured in both cooling and warming modes in the temperature range of 2−300 K is displayed in Figure 1, in which χ_m represents the molar magnetic susceptibility for one $[Ni(mnt)_2]^-$ unit of $[4'\text{-}CF_3bzPy][Ni(mnt)_2]$. The magnetic behavior of **1** is two magnetic susceptibility maxima and a surprisingly large thermal hysteresis loop in the χ_m versus T plot. Upon cooling, the χ_m value increases gradually, reaches the first maximum at around 169 K, and then drops abruptly. The second magnetic susceptibility maximum appears at around 50 K, and the magnetic susceptibility decreases exponentially below this temperature, the typical characteristic of a spin-gap system. During the warming process, the history dependence in the magnetic susceptibility occurs in the temperature range of 110−225 K, indicating thermally induced magnetic bistability. The width of the hysteresis loop in this bistable magnetic system was calculated as ~49 K on the basis of the peak temperatures in the $d\chi_m/dT$ versus T plot (see Figure 1b).

A large thermal hysteresis loop is commonly observed in the transition metal SCO complexes[23] and the cyano-bridged metal-to-metal charge-transfer complexes,[24] but located at organic radicals[7d,25] and metal−bisdithiolene complexes. To the best of our knowledge, only three other examples in metal−bisdithiolene complexes have been reported to show a more than 30 K hysteretic loop so far, namely, the 40 K hysteretic loop reported in $[Cp_2Co][Ni(tfadt)_2]$[11b] and the ~37 and ~60 K hysteretic loops observed in two polymorphs of $[NO_2bzql][Ni(dmit)_2]$ (where NO_2bzql^+ represents 1-(4-nitrobenzyl)-quinolinium).[26]

Crystal Structure in the High-Temperature (HT) Phase at 293, 190, and 160 K. Crystal **1** crystallizes in the triclinic space group $P\bar{1}$ at 293 K; its asymmetric unit comprises one $[Ni(mnt)_2]^-$ together with one $4'\text{-}CF_3bzPy^+$ (Figure 2). The bond lengths and angles in the planar anion are in good agreement with the values in the reported $[Ni(mnt)_2]^-$ compounds.[13,27] The characteristic dihedral angles in the Λ-shaped $4'\text{-}CF_3BzPy^+$ cation are 67.8° between the phenyl and pyridyl rings and 87.8° and 88.5° between the reference plane N(5)C(14)C(15) and the phenyl ring and the pyridyl ring, respectively. The CF_3 group is structurally disordered with two possible sites for each fluorine atom.

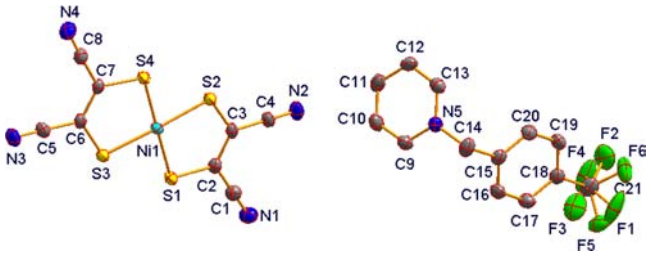

Figure 2. ORTEP view with non-hydrogen atom labeling and thermal ellipsoids drawn at the 20% probability level for **1** at 293 K. The structurally disordered CF_3 group has two possible sites.

As shown in Figure 3a,b, the anions and cations form mixed stacks, with alternating anionic dimers (AA) and cationic dimers (CC) in an ...AACCAACC... fashion, along the crystallographic $a + b$ direction. The mixed stacks are aligned into a molecular layer, which is parallel to the crystallographic (001) plane. Two cofacial $[Ni(mnt)_2]^-$ ions in an anionic dimer are related to each other via an inversion center, and their long molecular axes are parallel to each other. The slippage of two $[Ni(mnt)_2]^-$ anions along the long molecular axes leads to the existence of slightly longer interatomic separations of 4.119 Å for Ni(1)···Ni(1)#1, 4.053 Å for S(2)···S(3)#1, and 4.019 Å for Ni(1)···S(3)#1, with symmetric code #1 being $-x$, $1 - y$, $-z$. Two $4\text{-}CF_3bzPy^+$ ions in a cationic dimer are arranged in a chair conformation alignment. Two (trifluoromethyl)benzene moieties exhibit an antiparallel arrangement, and the phenyl rings are parallel to each other with a longer centroid-to-centroid separation of 4.823 Å. The phenyl ring in the cation moiety is superimposed over one of two chelate rings in the anion moiety with a dihedral angle of 5.9°.

The crystal structures of **1** at 190 and 160 K (not shown here) are quite analogous to that at 293 K. The characteristic bond parameters in the crystal structures at both temperatures are summarized in the Supporting Information.

Crystal Structure in the Low-Temperature (LT) Phase at 131 K. Upon cooling from 293 to 131 K, the space group of the crystal remains the same and the lengths of the a- and b-axes do not change remarkably, but the length of the c-axis is roughly doubled compared to that of the structure at 293 K, indicating that the asymmetric unit switches from one $[4'\text{-}CF_3bzPy][Ni(mnt)_2]$ pair in the HT phase to two $[4'\text{-}CF_3bzPy][Ni(mnt)_2]$ pairs in the LT phase (Figure 4). Even though the bond lengths and angles (Table S1, Supporting Information) in two planar anions are comparable to those at 293 K, the relative orientations between two crystallographically different anions/cations change significantly in the LT phase (Figure S5, Supporting Information). The mean molecular planes (defined by four S atoms) as well as the long molecular axes (defined by a straight line passing through the center of two C=C bonds of mnt^{2-} ligands) of two crystallographically independent anions make angles of 8.9° and 22.6°, respectively. For two crystallographically inequivalent cations, the characteristic dihedral angles are 71.1° (82.4°) between the phenyl and pyridyl rings and 83.7° (76.1°) and 59.2° (55.0°) between the reference plane and the phenyl ring

dx.doi.org/10.1021/ic302571p | Inorg. Chem. 2013, 52, 3870−3877

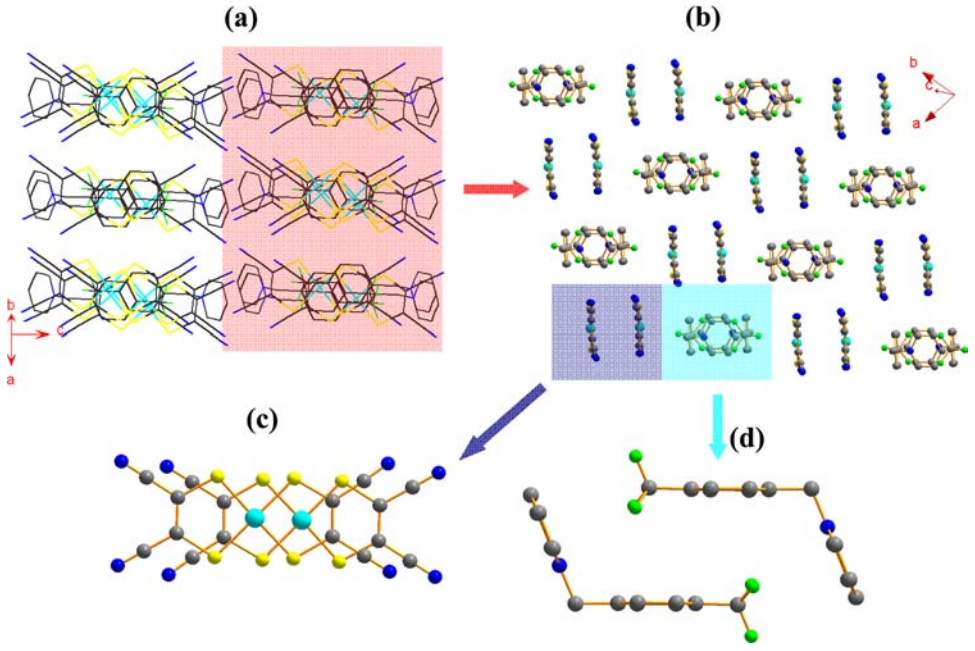

Figure 3. (a) Packing structure of **1** at 293 K projected along the crystallographic $a + b$ direction. (b) A monolayer, being parallel to the crystallographic (001) plane, shows the alternating stacks of dimeric anions and dimeric cations along the crystallographic $a + b$ direction. (c) Anionic dimer. (d) Cationic dimer.

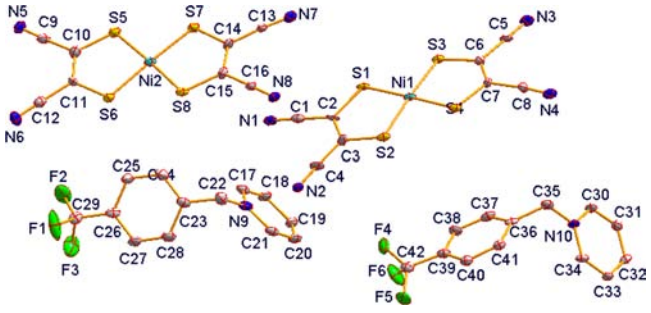

Figure 4. ORTEP view with non-hydrogen atom labeling and thermal ellipsoids drawn at the 20% probability level for **1** at 131 K.

and the pyridyl ring for the cation containing F4 (F1). Obviously, the dihedral angle between the reference plane and the pyridyl ring changes significantly in the conformation of the cations upon cooling from the HT to the LT phase. Additionally, the structurally disordered CF_3 group in the HT phase becomes ordered in the LT phase.

The packing structure of **1** in the LT phase is displayed in Figure 5. The phase transition results in a switch from one type of molecular layer to two types of crystallographically different molecular layers, comprised of, respectively, the Ni1 anions together with F4 cations (this layer is labeled as L-1) and the Ni2 anions together with F1 cations (this layer is labeled as L-2). The L-1 and L-2 molecular layers alternate in an ...L-1/L-2/L-1/L-2... manner along the *c*-axis direction, which is responsible for the lengthening of the *c*-axis at low temperature. The alignment of anions and cations is quite similar to that at 293 K in the L-1 layer (see Figures 3b and 5c), while distinct from that at 293 K in the L-2 layer (see Figure 5d). The molecular arrangement differences between the L-1 and L-2 layers are illustrated in Figure 5e,f and are as follows: (1) The significant slippage along the short molecular axis of the anion occurs between the neighboring anion and cation in the L-2 layer, and this slippage leads to a shift of the phenyl ring superimposed over one of two chelate rings in the L-1 layer away from the flat anion. (2) A rotation of the whole molecule, being relative to the anion plane, takes place for the cation in the L-2 layer, which gives rise to the phenyl ring tilting against the mean molecular plane of the anion (defined by four S atoms) with a dihedral angle of 36.5° in the L-2 layer versus 11.2° in the L-1 layer, while the corresponding dihedral angle is 5.9° in the crystal structure at 293 K. (3) The relative molecular orientation between the anions as well as between the cations in the neighboring molecular layers shows a significant change.

As analyzed above, the structural changes from the HT to the LT phase can be concluded to be the disorder-to-order transformation of the CF_3 groups and the dislocation motion between the L-1 and L-2 molecular layers.

Analysis of the Relationship between Structure and Magnetic Behavior. From a structural viewpoint, the dimer magnetic exchange models with one J constant and two different J constants are respectively chosen for the fit of the temperature-dependent magnetic susceptibility in the HT and LT phases, since there exist one and two types of crystallographically different π-type $[Ni(mnt)_2]_2^{2-}$ dimers in the HT and LT phases:

$$\chi_m = \frac{Ng^2\mu_B{}^2}{k_BT}\frac{1}{3 + \exp(-2J/k_BT)} + \frac{C}{T - \Theta} + \chi_0 \quad (1)$$

$$\chi_m = \frac{Ng^2\mu_B{}^2}{2k_BT}\left\{\frac{1}{3 + \exp(-2J_1/k_BT)} + \frac{1}{3 + \exp(-2J_2/k_BT)}\right\} + \frac{C}{T - \Theta} + \chi_0 \quad (2)$$

where the $C/(T - \Theta)$ term represents the uncoupled magnetic impurity and χ_0 is the temperature-independent magnetic susceptibility, which includes the diamagnetism originated from

dx.doi.org/10.1021/ic302571p | *Inorg. Chem.* 2013, 52, 3870−3877

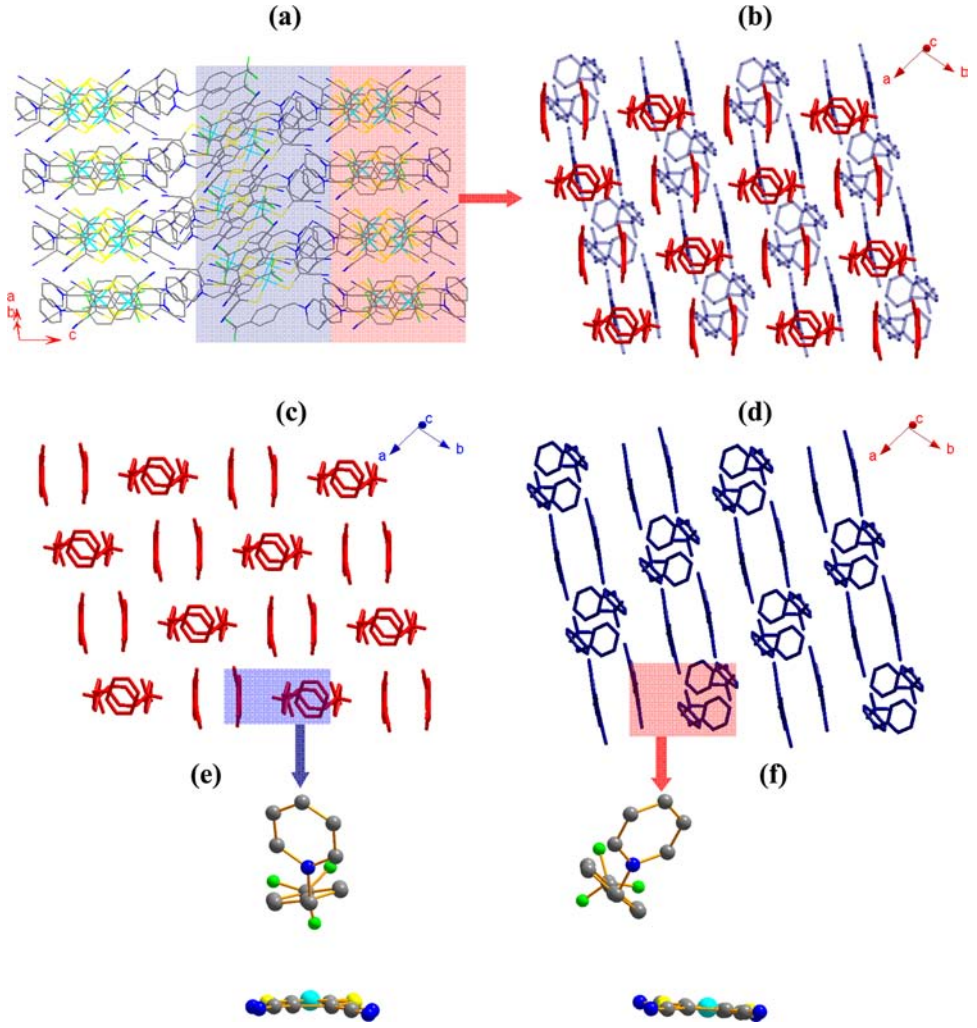

Figure 5. (a) Packing diagram of **1** at 131 K. (b) Two crystallographically independent layers, which are marked in red (containing Ni1-type anions and F4-type cations) and blue (containing Ni2-type anions and F1-type cations). Arrangements of anions and cations in the monolayer containing (c) Ni1-type anions and (d) Ni2-type anions. Relative alignment of the anion and cation with (e) Ni1-type anions and (f) Ni2-type anions.

the closed atom shells and possible van Vleck paramagnetism contributed by the coupling of the ground and excited states through a magnetic field. In the LT phase, the magnetic susceptibility in the temperature range of 1.8−130 K was fitted to eq 2 to yield the parameters $g = 1.991(8)$, $J_1/k_B = -43.4(1)$ K, $J_2/k_B = -268(9)$ K, $C = 7.9(3) \times 10^{-3}$ emu·K·mol^{-1}, $\Theta = -1.8(1)$ K, and $\chi_0 = -5.12(1) \times 10^{-4}$ emu·mol^{-1} with a ratio of J_2 to J_1 of ∼6.2. On the basis of the fitted Curie constant, the amount of $S = 1/2$ magnetic impurities, arising from the uncoupled spins, is estimated to be ca. 2%. In the HT phase, the temperature-dependent magnetic susceptibility in the temperature range of 167−300 K was fitted to eq 1, and the C, Θ, and χ_0 parameters remained the same as obtained from the fitting in the LT phase. The best fit gave $g = 2.02(2)$ and $J/k_B = -50.3(7)$ K. These results indicated that the antiferromagnetic (AFM) coupling interaction in the LT phase is approximately unchanged within one of two types of dimers whereas it is much stronger in the other one compared to that in the HT phase.

Mulliken spin population analyses based on the DFT calculations were performed for the dimers to identify the relationship between the structure and the magnetic behavior. Figure 6 presents the calculated Mulliken spin densities of the BS singlet state for the dimer in the HT phase and the Ni1 dimer in the LT phase. It is noted that (1) the unpaired electrons are predominantly delocalized throughout the anion skeleton, in which approximately 85% of the unpaired electron spins are localized on the NiS_4 core and the spin polarization with an alternation in sign of the spin density appears in the C−CN moieties of the mnt^{2-} ligands for each $[Ni(mnt)_2]^-$ anion within the dimer in the HT phase, (2) the α and β spins almost localize in two individual $[Ni(mnt)_2]^-$ anions in the dimer, indicating that the unpaired electrons between two individual $[Ni(mnt)_2]^-$ anions are magnetically coupled via a spin polarization mechanism in the HT phase, and (3) the calculated Mulliken spin population of the Ni1 dimer in the LT phase is similar to that of the dimer in the HT phase (see Figure 6a,b), while that of the Ni2 dimer in the LT phase is quite different from that of the dimer in the HT phase. The spin density in all the atoms is zero, suggesting a closed-shell configuration for the Ni2 dimer and clearly reflecting the strongly delocalized character of the two singly occupied π orbitals of the $[Ni(mnt)_2]^-$ anions; therefore, the unpaired electrons between two individual $[Ni(mnt)_2]^-$ anions are magnetically coupled via a spin delocalization mechanism. This situation is further identified from the frontier molecular orbitals of the BS singlet states of three spin dimers in the HT and LT phases. Figure 7 shows a stronger overlap between the

dx.doi.org/10.1021/ic302571p | Inorg. Chem. 2013, 52, 3870−3877

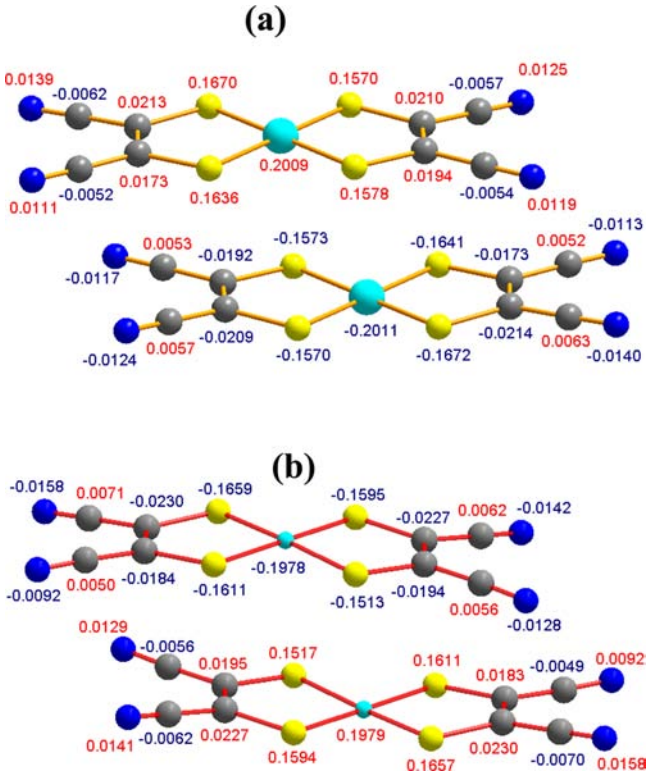

Figure 6. Spin density distribution in the BS singlet state of (a) the spin dimer in the HT phase and (b) the Ni1-type spin dimer in the LT phase.

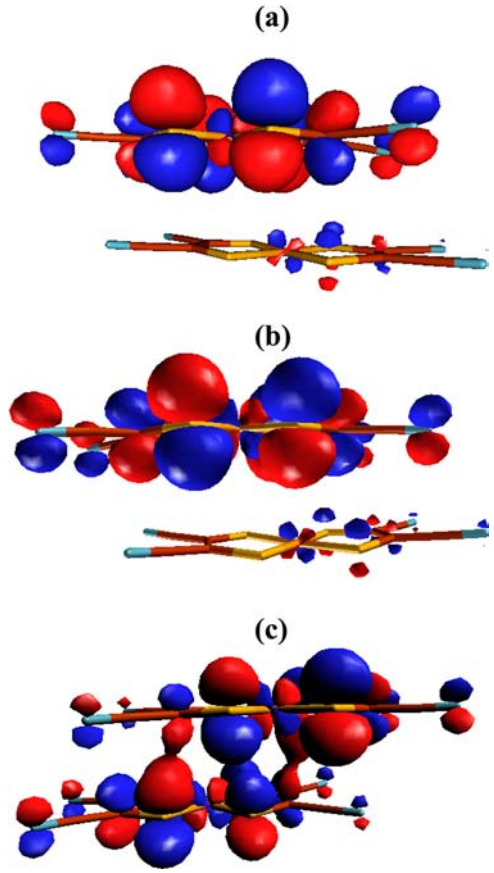

Figure 7. Kohn–Sham-type orbitals (HOMO) of the spin dimer (a) in the HT phase and (b, c) corresponding to the spin dimers with Ni1-type and Ni2-type anions in the LT phase, respectively.

orbitals of two $[Ni(mnt)_2]^-$ anions within the Ni2 dimer in the LT phase, but no significant orbital overlap for the dimer in the HT phase as well as for the Ni1 dimer in the LT phase, indicating the presence of a much stronger AFM exchange interaction within the Ni2 dimer and a relatively weaker AFM exchange interaction within the Ni1 dimer in the LT phase as well as a weaker AFM exchange interaction within the dimer in the HT phase, since the AFM exchange constant is proportional to the overlap integral of the orbitals.

Differential Scanning Calorimetry. The DSC plot of **1** is depicted in Figure 8, which shows a gradual endothermic peak around the transition temperature in the heating process, with an onset temperature of 200.2 K, a peak temperature $T_{max} \approx$ 211.4 K, and an endset temperature of 226.2 K. The peak temperature $T_{max} \approx 211.4$ K is close to the T_C obtained from the magnetic susceptibility measurement. The enthalpy change (ΔH), calculated from the integrated peak area, is estimated to be only 282.6 J·mol^{-1} for **1**. Such a small enthalpy change means that the difference in lattice energy between the HT and LT phases is very small.

Cooperativity of the Magnetic Phase Transition. The width of thermal hysteresis loop is a technologically crucial parameter for practical applications of the magnetic bistability. In general, the width of the thermal hysteresis loop is related to the cooperative effects and becomes larger as the cooperativity of the magnetic phase transition increases. A variety of cooperative effects are widespread in the different magnetic bistability systems; for example, the bond distance changes in the coordination sphere of a spin-active metal ion usually cooperate with the spin-crossover process in an SCO complex. It was also observed that the coordination bond formation/dissociation cooperates with the hysteresis magnetic phase

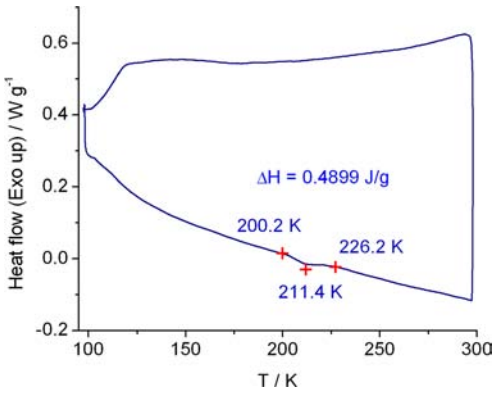

Figure 8. DSC curve for **1** showing the T_{onset}, T_{max}, T_{endset}, and latent heat ΔH of the phase transition.

transition in $(BDTA)_2[Co(mnt)_2]$[28a] and $Na[Ni(pdt)_2]\cdot 2H_2O$.[28b] The disorder-to-order transformation of the spin-inactive components, CF_3 and cyclopentadienyl groups, couples with the magnetic bistability in $[Cp_2M][Ni(tfadt)_2]$ (M = Fe or Co) complexes.[11] Furthermore, the rupture of the C–H$\cdots\pi$ interactions between the neighboring dimers and the large-amplitude motion of the phenalenyl rings assist in the magnetic bistability in the charge delocalization spirobiphenalenyl neutral radical conductors.[29] The disorder-to-order transformation of the spin-inactive component CF_3 and the dislocation motion of the neighboring molecular layers couple with the magnetic bistability in **1**.

dx.doi.org/10.1021/ic302571p | Inorg. Chem. 2013, 52, 3870–3877

CONCLUDING REMARKS

In summary, we presented a novel magnetic bistable example which shows a surprisingly large thermal hysteresis loop but no strong intermolecular interaction in the lattice. To the best of our knowledge, this is the first example of an isolated metal−bisdithiolene dimer system that displays a spin transition and, moreover, with a wide hysteresis loop. In this study, it was proposed that the lattice reorganization stemming from the change of the bond parameters or motion of groups/molecules during a magnetic phase transition cooperates kinetically with the thermal hysteresis effect, and the higher energy barrier for the lattice reorganization in this example is responsible for the wider thermal hysteresis loop. This finding demonstrated that a larger hysteresis loop magnetic bistability system is only found in a compound with a greater lattice reorganization energy between the thermodynamically stable phases and the transition state.

ASSOCIATED CONTENT

Supporting Information

Tables giving the characteristic bond lengths and angles in the $[Ni(mnt)_2]^-$ moiety of **1** at different temperatures, significant interatomic separations of dimer anions in the crystals of **1** at different temperatures, and characteristic dihedral angles in the cation moiety of **1**, figures showing ORTEP views with non-hydrogen atom labeling and thermal ellipsoids drawn at the 20% probability level for **1** at 160 and 190 K, packing diagrams of **1** at 160 and 190 K viewed along the $a + b$ direction, an illustration of the relative orientations between two crystallographic inequivalent anions and cations for **1** at 131 K, two types of anion dimers in the crystal structure at 131 K, and variable-temperature EPR spectra upon cooling and heating, and CIF data for **1**. This material is available free of charge via the Internet at http://pubs.acs.org.

AUTHOR INFORMATION

Corresponding Author

*Phone: +86 25 58139476. Fax: +86 25 58139481. E-mail: xmren@njut.edu.cn (X.-M.R.), zhousm@ustc.edu.cn (S.-M.Z.).

Notes

The authors declare no competing financial interest.

ACKNOWLEDGMENTS

We thank the Priority Academic Program Development of Jiangsu Higher Education Institutions and National Natural Science Foundation of China (Grants 91122011 and 21071080) for financial support. X.-M.R. thanks Prof. C. J. Fang for reading this manuscript.

REFERENCES

(1) (a) Kahn, O.; Martinez, C. J. *Science* **1998**, *279*, 44−48. (b) Galet, A.; Gaspar, A. B.; Muñoz, M. C.; Bukin, G. V.; Levchenko, G.; Real, J. A. *Adv. Mater.* **2005**, *17*, 2949−2953. (c) Sato, O.; Tao, J.; Zhang, Y. Z. *Angew. Chem., Int. Ed.* **2007**, *46*, 2152−2187.

(2) (a) Lin, J. B.; Xue, W.; Wang, B. Y.; Tao, J.; Zhang, W. X.; Zhang, J. P.; Chen, X. M. *Inorg. Chem.* **2012**, *51*, 9423−9430. (b) Hayami, S.; Kato, K.; Komatsu, Y.; Fuyuhiro, A.; Ohba, M. *Dalton Trans.* **2011**, 2167−2169. (c) Roubeau, O.; Castro, M.; Burriel, R.; Haasnoot, J. G.; Reedijk, J. *J. Phys. Chem. B* **2011**, *115*, 3003−3012.

(3) (a) Hayami, S.; Urakami, D.; Kojima, Y.; Yoshizaki, H.; Yamamoto, Y.; Kato, K.; Fuyuhiro, A.; Kawata, S.; Inoue, K. *Inorg. Chem.* **2010**, *49*, 1428−1432. (b) Li, B.; Wei, R. J.; Tao, J.; Huang, R. B.; Zheng, L. S.; Zheng, Z. P. *J. Am. Chem. Soc.* **2010**, *132*, 1558−1566.

(4) (a) Kepenekian, M.; Guennic, B. L.; Robert, V. *J. Am. Chem. Soc.* **2009**, *131*, 11498−11502. (b) Southon, P. D.; Liu, L.; Fellows, E. A.; Price, D. J.; Halder, G. J.; Chapman, K. W.; Moubaraki, B.; Murray, K. S.; Létard, J. F.; Kepert, C. J. *J. Am. Chem. Soc.* **2009**, *131*, 10998−11009. (c) Neville, S. M.; Halder, G. J.; Chapman, K. W.; Duriska, M. B.; Moubaraki, B.; Murray, K. S.; Kepert, C. J. *J. Am. Chem. Soc.* **2009**, *131*, 12106−12108.

(5) (a) Muñoz, M. C.; Real, J. A. *Coord. Chem. Rev.* **2011**, *255*, 2068−2093. (b) Ohtani, R.; Yoneda, K.; Furukawa, S.; Horike, N.; Kitagawa, S.; Gaspar, A. B.; Muñoz, M. C.; Real, J. A.; Ohba, M. *J. Am. Chem. Soc.* **2012**, *133*, 8600−8605. (c) Adams, C. J.; Muñoz, M. C.; Waddington, R. E.; Real, J. A. *Inorg. Chem.* **2011**, *50*, 10633−10642. (d) Rodríguez-Velamazán, J. A.; González, M. A.; Real, J. A.; Castro, M.; Muñoz, M. C.; Gaspar, A. B.; Ohtani, R.; Ohba, M.; Yoneda, K.; Hijikata, Y.; Yanai, N.; Mizuno, M.; Ando, H.; Kitagawa, S. *J. Am. Chem. Soc.* **2012**, *134*, 5083−5089. (e) Białońska, A.; Bronisz, R. *Inorg. Chem.* **2012**, *51*, 12630−12637.

(6) (a) Leeladee, P.; Baglia, R. A.; Prokop, K. A.; Latifi, R.; De Visser, S. P.; Goldberg, D. P. *J. Am. Chem. Soc.* **2012**, *134*, 10397−10400. (b) Tao, J.; Maruyama, H.; Sato, O. *J. Am. Chem. Soc.* **2006**, *128*, 1790−1791. (c) Yoshida, Y.; Tanaka, H.; Saito, G.; Ouahab, L.; Yoshida, H.; Sato, N. *Inorg. Chem.* **2009**, *48*, 9989−9991. (d) Shimamoto, N.; Ohkoshi, S.-i.; Sato, O.; Hashimoto, K. *Inorg. Chem.* **2002**, *41*, 678−684.

(7) (a) Ren, X. M.; Nishihara, S.; Akutagawa, T.; Noro, S.; Nakamura, T.; Fujita, W.; Awaga, K. *Chem. Phys. Lett.* **2006**, *418*, 423−427. (b) Willett, R. D.; Gomez-Garcia, C. J.; Ramakrishna, B. L.; Twamley, B. *Polyhedron* **2005**, *24*, 2232−2237. (c) Brusso, J. L.; Clements, O. P.; Haddon, R. C.; Itkis, M. E.; Leitch, A. A.; Oakley, R. T.; Reed, R. W.; Richardson, J. F. *J. Am. Chem. Soc.* **2004**, *126*, 8256−8265. (d) Fujita, W.; Awaga, K. *Science* **1999**, *286*, 261−262.

(8) (a) Kahn, O.; Codjovi, E.; Garcia, Y.; van Koningsbruggen, P. J.; Lapayoudi, R.; Sommier, L. *ACS Symp. Ser.* **1996**, *644*, 298−310. (b) Real, J. A.; Andres, E.; Munoz, C. M.; Julve, M.; Granier, T.; Bousseksou, A.; Varret, F. *Science* **1995**, *268*, 265−267. (c) Matouzenko, G. S.; Molnar, G.; Brefuel, N.; Perrin, M.; Bousseksou, A.; Borshch, S. A. *Chem. Mater.* **2003**, *15*, 550−556. (d) Matouzenko, G. S.; Perrin, M.; Guennic, B.; Genre, C.; Molnar, G.; Bousseksou, A.; Borshch, S. A. *Dalton Trans.* **2007**, 934−942.

(9) (a) Lara, F. J. M.; Gaspar, A. B.; Aravena, D.; Ruiz, E.; Muñoz, M. C.; Ohba, M.; Ohtani, R.; Kitagawa, S.; Real, J. A. *Chem. Commun.* **2012**, *48*, 4686−4688. (b) Kepenekian, M.; Guennic, B. L.; Robert, V. *J. Am. Chem. Soc.* **2009**, *131*, 11498−11502. (c) Hayami, S.; Gu, Z. Z.; Yoshiki, H.; Fujishima, A.; Sato, O. *J. Am. Chem. Soc.* **2001**, *123*, 11644−11650.

(10) (a) Murray, K. S. *Eur. J. Inorg. Chem.* **2008**, 3101−3121. (b) Bauer, W.; Dirtu, M. M.; Garcia, Y.; Weber, B. *CrystEngComm* **2012**, *14*, 1223−1231.

(11) (a) Jeannin, O.; Clérac, R.; Fourmigué, M. *Chem. Mater.* **2007**, *19*, 5946−5964. (b) Jeannin, O.; Clérac, R.; Fourmigué, M. *J. Am. Chem. Soc.* **2006**, *128*, 14649−14656. (c) Jeannin, O.; Clérac, R.; Fourmigué, M. *CrystEngComm* **2007**, *9*, 488−495.

(12) Davison, A.; Holm, H. R. *Inorg. Synth.* **1967**, *10*, 8−33.

(13) Ren, X. M.; Meng, Q. J.; Song, Y.; Lu, C. S.; Hu, C. J. *Inorg. Chem.* **2002**, *41*, 5686−5692.

(14) *CrysAlis V1.171*; Oxford Diffraction Ltd.: Wrocław, Poland, 2004.

(15) Sheldrick, G. M. *SHELXL-97, Program for the Refinement of Crystal Structures*; University of Göttingen: Göttingen, Germany, 1997.

(16) Frisch, M. J.; Trucks, G. W.; Schlegel, H. B.; Scuseria, G. E.; Robb, M. A.; Cheeseman, J. R.; Zakrzewski, V. G.; Montgomery, J. A., Jr.; Stratmann, R. E.; Burant, J. C.; Dapprich, S.; Millam, J. M.; Daniels, A. D.; Kudin, K. N.; Strain, M. C.; Farkas, O.; Tomasi, J.; Barone, V.; Cossi, M.; Cammi, R.; Mennucci, B.; Pomelli, C.; Adamo, C.; Clifford, S.; Ochterski, J.; Petersson, G. A.; Ayala, P. Y.; Cui, Q.; Morokuma, K.; Malick, D. K.; Rabuck, A. D.; Raghavachari, K.; Foresman, J. B.; Cioslowski, J.; Ortiz, J. V.; Stefanov, B. B.; Liu, G.; Liashenko, A.; Piskorz, P.; Komaromi, I.; Gomperts, R.; Martin, R. L.; Fox, D. J.; Keith, T.; Al-Laham, M. A.; Peng, C. Y.; Nanayakkara, A.; Gonzalez,

C.; Challacombe, M.; Gill, P. M. W.; Johnson, B. G.; Chen, W.; Wong, M. W.; Andres, J. L.; Head-Gordon, M.; Replogle, E. S.; Pople, J. A. *Gaussian 98*, revision A.11; Gaussian, Inc.: Pittsburgh, PA, 2001.
(17) Becke, A. D. *Phys. Rev. A* **1988**, *38*, 3098−3100.
(18) Burke, K.; Perdew, J. P.; Wang, Y. In *Electronic Density Functional Theory: Recent Progress and New Directions*; Dobson, J. F., Vignale, G., Das, M. P., Eds.; Plenum Publishing Corp.: New York, 1998.
(19) Perdew, J. P. In *Electronic Structure of Solids*; Ziesche, P., Eschrig, H., Eds.; Akademie Verlag: Berlin, 1991; p 11.
(20) Perdew, J. P.; Chevary, J. A.; Vosko, S. H.; Jackson, K. A.; Pederson, M. R.; Singh, D. J.; Fiolhais, C. *Phys. Rev. B* **1992**, *46*, 6671−6687.
(21) Perdew, J. P.; Chevary, J. A.; Vosko, S. H.; Jackson, K. A.; Pederson, M. R.; Singh, D. J.; Fiolhais, C. *Phys. Rev. B* **1993**, *48*, 4978.
(22) Perdew, J. P.; Burke, K.; Wang, Y. *Phys. Rev. B* **1996**, *54*, 16533−16539.
(23) (a) Dorbes, S.; Valade, L.; Real, J. A.; Faulmann, C. *Chem. Commun.* **2005**, 69−71. (b) Dirtu, M. M.; Neuhausen, C.; Naik, A. D.; Rotaru, A.; Spinu, L.; Garcia, Y. *Inorg. Chem.* **2010**, *49*, 5723−5736. (c) Galán-Mascarós, J. R.; Coronado, E.; Forment-Aliaga, A.; Monrabal-Capilla, M.; Pinilla-Cienfuegos, E.; Ceolin, M. *Inorg. Chem.* **2010**, *49*, 5706−5714. (d) Adams, C. J.; Muñoz, M. C.; Waddington, R. E.; Real, J. A. *Inorg. Chem.* **2011**, *50*, 10633−10642.
(24) Ohkoshi, S.-i.; Matsuda, T.; Tokoro, H.; Hashimoto, K. *Chem. Mater.* **2005**, *17*, 81−84.
(25) Itkis, M. E.; Chi, X.; Cordes, A. W.; Haddon, R. C. *Science* **2002**, *296*, 1443−1445.
(26) Zang, S. Q.; Ren, X. M.; Su, Y.; Song, Y.; Tong, W. J.; Ni, Z. P.; Zhao, H. H.; Gao, S.; Meng, Q. J. *Inorg. Chem.* **2009**, *48*, 9623−9630.
(27) (a) Pei, W. B.; Wu, J. S.; Tian, Z. F.; Ren, X. M.; Song, Y. *Inorg. Chem.* **2011**, *50*, 3970−3980. (b) Tian, Z. F.; Duan, H. B.; Ren, X. M.; Lu, C. S.; Li, Y. Z.; Zhu, H. Z.; Meng, Q. J. *J. Phys. Chem. B* **2009**, *113*, 8278−8283. (c) Ren, X. M.; Nishihara, S.; Akutagawa, T.; Noro, S.; Nakamura, T. *Inorg. Chem.* **2006**, *45*, 2229−2234.
(28) (a) Umezono, Y.; Fujita, W.; Awaga, K. *J. Am. Chem. Soc.* **2006**, *128*, 1084−1085. (b) Takaishi, S.; Ishihara, N.; Kubo, K.; Katoh, K.; Breedlove, B. K.; Miyasaka, H.; Yamashita, M. *Inorg. Chem.* **2011**, *50*, 6405−6407.
(29) Pal, S. K.; Bag, P.; Sarkar, A.; Chi, X.; Itkis, M. E.; Tham, F. S.; Donnadieu, B.; Haddon, R. C. *J. Am. Chem. Soc.* **2010**, *132*, 17258−17264.